Transport Discovery of Emerging Robust Helical Surface States in $Z_2 = 0$ Systems

Hua Jiang,[1] Haiwen Liu,[2,3] Ji Feng,[2,3,*] Qingfeng Sun,[2,3] and X. C. Xie[2,3,†]
[1]Department of Physics and Jiangsu Key Laboratory of Thin Films, Soochow University, Suzhou 215006, China
[2]International Center for Quantum Materials, Peking University, Beijing 100871, China
[3]Collaborative Innovation Center of Quantum Matter, Beijing 100871, China
(Received 23 November 2013; revised manuscript received 10 March 2014; published 2 May 2014)

We study the possibility of realizing robust helical surface states in $Z_2 = 0$ systems. We find that the combination of anisotropy and finite-size confinement leads to the emergence of robust helical edge states in both two-dimensional and three-dimensional $Z_2 = 0$ systems. By investigating an anisotropic Bernevig-Hughes-Zhang model in a finite sample, we demonstrate that the transport manifestation of the surface states is robust against nonmagnetic disorder, resembling that of a $Z_2 = 1$ phase. Notably, the effective energy gap of the robust helical states can be efficiently engineered, allowing for potential applications as valley filters and valley valves. The realization of emerging robust helical surface states in realistic materials is also discussed.

DOI: 10.1103/PhysRevLett.112.176601 PACS numbers: 72.25.Dc, 73.20.-r, 73.43.-f, 73.63.-b

Introduction.—Two-dimensional (2D) quantum spin Hall effect (QSHE) and three-dimensional (3D) strong topological insulators (STIs), characterized by the time-reversal (TR) invariant $Z_2 = 1$, have generated extensive interest in recent years [1,2]. The hallmark of these novel phases is the existence of odd pairs of helical edge (2D) or surface (3D) states that are robust against TR-conserving perturbations. In 2D, the robust helical edge states give rise to quantized local and nonlocal conductance [3–5] and spin polarized edge current [6]. In 3D, the robust helical surface states with spin-momentum locked gapless dispersion [7,8] lead to half-integer quantum Hall effect [9], weak anti-localization [10], absence of backscattering [11], etc. [1]. These exotic properties make their host systems ideal platforms for testing fundamental physical paradigms and achieving promising application in low-power dissipation information processing.

However, the requirement of $Z_2 = 1$ for the existence of robust helical surface or edge states is rather stringent. Indeed, the QSHE is only experimentally confirmed in HgTe/CdTe and InAs/GaSb quantum wells [3,5]. The scarcity of host systems represents a materials challenge, hindering the study and development of devices based on robust helical edge states. In 3D systems, one may note other classes of TIs that harbor multiple Dirac surface states: $Z_2 = 0$ weak topological insulators (WTIs) [12–16] and topological crystalline insulators [17–22]. More recently, a WTI material $Bi_{14}Rh_3I_9$ was successfully fabricated in experiment, which generated intense attention [23]. It becomes highly desirable to be able to engineer these materials with multiple Dirac states into structures with robust topological transport.

In this Letter, we show the emergence of robust helical edge (surface) states in both 2D and 3D $Z_2 = 0$ systems, arising from anisotropic confinement in a finite-size sample. On the basis of transport simulations of an anisotropic Bernevig-Hughes-Zhang (BHZ) model, we demonstrate quantized conductance of helical edge states under strong nonmagnetic disorders. The robustness of helical surface states due to anisotropic confinement is generalizable to 3D WTIs. Moreover, the proposed $Z_2 = 0$ systems possess additional exotic properties not present in $Z_2 = 1$ TIs. In particular, by controlling the sample size and strain-engineered anisotropy, this mechanism allows for efficient tuning of the effective energy gap and the fabrication of valley filter and valley valve without breaking TR symmetry. Finally, two realistic material systems that host emerging robust helical surface states are proposed.

2D model.—We consider an anisotropic BHZ model in a square lattice [24,25]. The four-band tight-binding Hamiltonian in the momentum representation reads

$$\mathcal{H}(\vec{k}) = \begin{pmatrix} h(\vec{k}) & 0 \\ 0 & h^*(-\vec{k}) \end{pmatrix},$$

$$\begin{aligned} h(\vec{k}) = {} & \tau_z(m - m_x - m_y + m_x \cos k_x + m_y \cos k_y) \\ & + \tau_x v_x \sin k_x + \tau_y v_y \sin k_y, \end{aligned} \tag{1}$$

where $h(\vec{k})$ and its time reversal $h^*(-\vec{k})$ are, respectively, decoupled Hamiltonians for the two spins. The Pauli matrices $\vec{\tau}$ address the orbital space. This model involves five parameters. Specifically, m determines the band gap, $v_{x,y}$ reflects the Fermi velocity, and $m_{x,y}$ represent the hopping amplitudes between nearest-neighbor sites along the x, y directions, respectively. The gap parameter m is a key variable in subsequent simulations. We adopt the following values for the other parameters unless otherwise specified: $m_x = 0.8$, $m_y = 1.2$, $v_x = v_y = 3.0$.

We first examine the topological properties of bulk phase described by this model by calculating the Z_2 invariant [12]. A $Z_2 = 1$ QSHE is obtained when $m \in (0, 2m_x) \cup (2m_y, 2m_x + 2m_y)$ [24,25]. In contrast, $Z_2 = 0$ when $m \in (-\infty, 0) \cup (2m_x + 2m_y, \infty)$ or $m \in (2m_x, 2m_y)$. However, the two regions with $Z_2 = 0$ are distinct from each other. When $m \in (-\infty, 0) \cup (2m_x + 2m_y, \infty)$, all bands are normal bands as ordinary insulator, whereas the region $m \in (2m_x, 2m_y)$ is nontrivial in the case of anisotropic $m_x \neq m_y$. It contains two inverted bands around $k_x = 0$ and π (see the Supplemental Material for details [26–29]). The inverted bands guarantee the existence of helical edge modes, whose amplitude decays from y boundary to the bulk exponentially with a decay length $\xi \sim 2v_y/\Delta^b$. Here, Δ^b denotes the inverted bulk gap [30]. When $m \in (2m_x, 2m_y)$, the two inverted gaps ($\Delta_0^b = 4m_y - 2m$ at $k_x = 0$, $\Delta_\pi^b = 2m - 4m_x$ at $k_x = \pi$) result in two pairs of helical edge modes labeled by 0 and π, respectively.

Narrow width or thickness of a $Z_2 = 1$ TI is often viewed to impose adverse effects on the transport of helical surface states. In a 2D system, the edge channels on the two sides of a narrow sample becomes hybridized, leading to undesirable backscattering between edge states by weak disorder [30]. In a 3D system, the high-quality samples are always grown via layer-by-layer MBE techniques. It was indeed observed in ultrathin films that the finite size effect leads to a hybridization gap, destroying the robustness of the helical surface state and drastically diminishing the surface conductivity [31].

Key to our proposal is the observation that in a finite sample, these two helical edge states behave differently for various m values [see Figs. 1(a) and 1(b)]. Intriguingly, when m approaches the critical value corresponding to the topological phase transition (i.e., $m = 1.64$), the bulk gap at π approaches zero, $\Delta_\pi^b \to 0$, while Δ_0^b remains finite. Consequently, the decay length ξ_π of π helical edge channels is exponentially long, whereas ξ_0 of 0 helical edge channels can, in principle, be much smaller than the sample width. The strong hybridization of π helical edge states annihilates the corresponding edge channels, whereas the small ξ_0 value guarantees the survival of 0 helical edge channels. Therefore, from a transport point of view as shown in Fig. 1(b), the conducting edge channels are similar to those in Fig. 1(c), although their Z_2 invariants defined for the bulk systems are different. Besides, there are two pairs of conducting channels in Fig. 1(a), despite the fact that $Z_2 = 0$. The similarity between conducting edge channels between the $Z_2 = 0$ system [Fig. 1(b)] and the $Z_2 = 1$ system [Fig. 1(c)] leads naturally to the speculation that the emergent $k_x = 0$ helical edge states are as robust as the edge states in a $Z_2 = 1$ system.

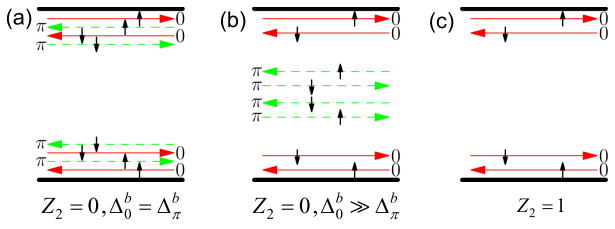

FIG. 1 (color online). [(a)– (c)] Schematic plots of helical edge modes in the anisotropic BHZ stripe with y termination, for $m = 2.00, 1.64, 1.56$. The vertical arrows represent electron spin. In subplot (b), the helical edge channels around $k_x = \pi$ are hybridized due to finite size confinement, leaving one pair of helical edge channels around $k_x = 0$. Thus, these conducting channels resemble subplot (c).

In order to quantitatively assess the robustness of those emerging $Z_2 = 0$ helical edge states, we inspect a two-terminal device and a π-bar device [see Figs. 2(a) and 2(e)] and study their transport properties in the presence of TR-conserving disorder using the Landauer-Büttiker formula [32–34]. The longitudinal terminals are perfect leads with the same parameters as the central region, and the transverse terminals are metallic leads. The disorder is modeled by the Anderson-type random on-site potential uniformly distributed in the range $[-W/2, W/2]$. As in the experimental setup [3,5], the two-terminal conductance $G_{12,12}$ and nonlocal conductance $G_{14,23}$ values of these two devices are systematically assayed in our simulations.

In Figs. 2(b)–2(d), the two-terminal conductance $G_{12,12}$ and the corresponding fluctuation versus Fermi energy ϵ_F under various m are plotted. The case of emergent helical states with $m = 1.64$ is shown in Fig. 2(c). The conductance $G_{12,12}$ shows two quantized plateaus $4e^2/h$ and $2e^2/h$ in the clean limit. In the presence of strong disorder, the $4e^2/h$ conductance decreases rapidly while the $2e^2/h$ plateau remains unchanged with vanishing fluctuation. Therefore, the two-terminal transport properties of emergent helical edge states in the $Z_2 = 0$ case behave exactly like a $Z_2 = 1$ QSHE, as shown in Figs. 2(c) and 2(d). The conductance is completely different from the $Z_2 = 0$, $\Delta_0^b = \Delta_\pi^b$ case, where only the $G_{12,12} = 4e^2/h$ plateau is present in the clean limit, which is found to be fragile against disorder [see Fig. 2(b)]. This is because the carriers can scatter between the counterpropagating 0 and π channels in this case [see Fig. 1(a)]. In contrast, due to the vanishing of π helical edge states under finite size confinement, the emergent helical states described above are not susceptible to these scattering channels.

The two-terminal measurements can also be corroborated by π-bar measurements [see Figs. 2(f)–2(h)]. For the case with emergent helical edge states, $G_{14,23}$ shows well quantized plateaus at $4e^2/h$, irrespective of leads detail and strong disorder strength [see Fig. 2(g)]. The two-terminal perfect $2e^2/h$ plateau and π-bar perfect $4e^2/h$ conductance plateaus should plausibly lead to a transport definition of robust helical edge states in these $Z_2 = 0$ systems. In a $Z_2 = 1$ topological insulator, the robustness of the edge conduction is derived from its intrinsic topological character. The robust helical edge states in our $Z_2 = 0$ model,

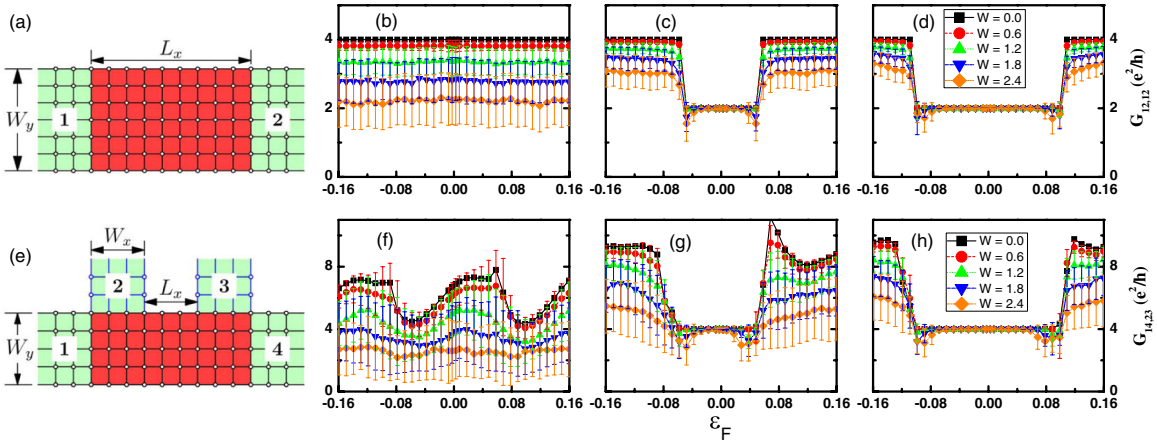

FIG. 2 (color online). [(a),(e)] Schematic plot of two-terminal and π-bar devices . The disorder is considered in the central (red) region. The size parameters are $L_x = 120$, $W_x = 120$, $W_y = 60$. [(b)–(d)] Two-terminal conductance values $G_{12,12}$ of device (a); [(f)–(h)] nonlocal conductance values $G_{14,23}$ of device (e) versus Fermi energy ϵ_F for different disorder strengths W at various $m = 2.00$ [(b),(f)], 1.64 [(c),(g)], 1.56 [(d),(h)]. The error bars denote the conductance fluctuation.

on the other hand, arise from the fact that the intervalley scattering is detuned by the hybridization gap of one of the valleys.

Besides the emergence of robust helical edge states in the $Z_2 = 0$ system, which conveniently augments the scope of study confined in QSHE, our proposal also has certain advantages over the helical states in $Z_2 = 1$ systems. For example, the energy window with robust edge channel in our proposed model can be easily engineered via the tailoring of the sample width, whereas such a window in the $Z_2 = 1$ system is difficult to change in experiments. Figure 3 plots two-terminal conductance $G_{12,12}$ as a function of ϵ_F under various sample widths W_y for these two systems. With increasing W_y, in the $Z_2 = 0$ system the energy window with robust $2e^2/h$ plateau continuously decreases from a moderate value to zero [see Figs. 3(a) and 3(b)]. In contrast, the window of plateau in the $Z_2 = 1$ system is basically equal to bulk gap and insensitive to the width variation [see Figs. 3(c) and 3(d)]. To be specific, the energy window, which is appropriately termed an effective energy gap, in Fig. 3(a) arises from the hybridization gap of the π helical edge states and can be continuously tuned by tailoring the sample width [see Fig. 3(b)].

3D model.—Similar phenomena also exist in 3D anisotropic WTIs. We take the anisotropic Wilson-Dirac-type model as an example [35–40]. The Hamiltonian in a cubic lattice reads

$$\mathcal{H}(\vec{k}) = m(\vec{k})\sigma_0 \otimes \tau_z + \sum_\alpha \upsilon_\alpha \sin k_\alpha \sigma_\alpha \otimes \tau_x,$$
$$m(\vec{k}) = m + \sum_\alpha m_\alpha(\cos k_\alpha - 1), \quad (2)$$

where σ are the Pauli matrices in spin space, and $\alpha = x, y, z$. Parameters τ, m, υ_α, m_α have the same meanings as in the 2D model of Eq. (1). Recently, several works have studied the finite size effect and transport properties of 3D WTIs [35–39]. These works focus on two cases: (i) isotropic bulk, i.e., $m_x = m_y = m_z$; (ii) anisotropic bulk but isotropic xy surface, i.e., $m_x = m_y \neq m_z$. Interestingly, we find the combined effects of finite size confinement and anisotropic surface, i.e., $m_x \neq m_y$, leads to a unique phenomenon in the xy surface. The anisotropy may be induced by elastic strain engineering. For example, when an isotropic WTI film is deposited to a substrate with uniform tensile (compressive) strain along the x direction, the anisotropic WTI with $m_x < m_y$ ($m_x > m_y$) is obtained [see, respectively, regions II and IV in Fig. 4(d)]. Henceforth, both tensile and compressive strains are explored in terms of relative values of m_x and m_y, whereas other parameters are fixed: $m = 2.26$, $m_z = 0.8$, $\upsilon_x = \upsilon_y = \upsilon_z = 1.5$.

Figures 4(a)–(c) schematically display the evolution of surface energy bands of the anisotropic WTI film. For

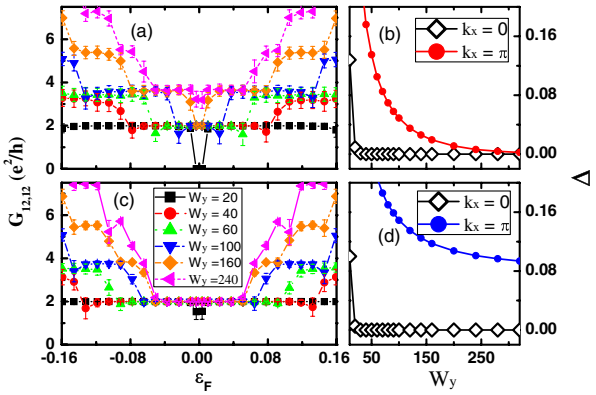

FIG. 3 (color online). [(a),(c)] The two-terminal conductance $G_{12,12}$ versus Fermi energy ϵ_F for different sample widths W_y at various $m = 1.64$ (a), 1.56 (c), with $L_x = 120$ and $W = 1.8$. [(b),(d)] Finite size energy gap Δ of $k_x = 0(\pi)$ as a function of W_y at fixed $m = 1.64$ (b) and 1.56 (d).

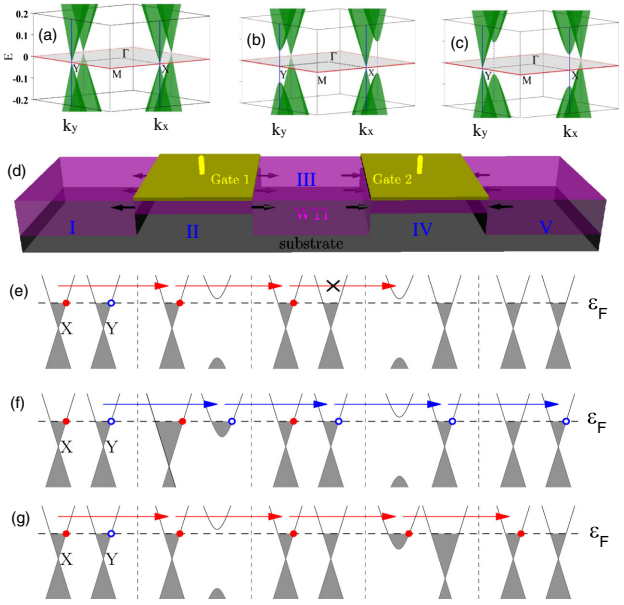

FIG. 4 (color online). [(a)–(c)] The surface energy bands of anisotropic WTI film with parameters (a) $m_x = 0.9$, $m_y = 1.1$, $N_z = 120$; (b) $m_x = 0.9$, $m_y = 1.1$, $N_z = 20$; (c), $m_x = 1.1$, $m_y = 0.9$, $N_z = 20$. N_z is the sample thickness. (d) Schematic diagram of the valley filter and valley valve device. The Fermi energy in region II (IV) can be tuned by the attached gates. The black arrows with in (out) direction represent the tensile (compressive) strain. [(e)–(h)] Schematic plots of the working mechanisms for the device. Open (filled) circles denote the electrons in $X(Y)$ valleys.

sufficiently thick films, two gapless helical surface modes with Dirac cone $X(0,\pi)$ and $Y(\pi,0)$ exist at the top surface [see Fig. 4(a)]. X, Y are two valleys analogous to K and K' in graphene. In thinner films, the finite size confinement leads to hybridization gaps in helical surface states. As shown in Fig. 4(b), the valley X remains almost gapless while the hybridization gap Δ_Y^s at valley Y is remarkable. This peculiar feature arises from the fact that the coupling strength of surface state at X is much weaker than that at Y, which is due to bulk inverted gaps satisfying $\Delta_X^b = 2m - 4m_x \gg \Delta_Y^b = 2m - 4m_y$ in tensile strained WTI film. Similar to the 2D case, when ϵ_F is located inside the hybridization gap of the Y valley, the X helical surface states survive, and intervalley scattering is definitely avoided. In other words, the emerging X helical surface states are robust and share the common features of those states in STIs. Moreover, the energy window (effective energy gap) with robust conducting states can be engineered via varying the sample thickness. Specifically, the gapped Y valley case and the gapped X valley case can interconvert by changing the system from tensile strain to compressive strain [see Fig. 3(c)].

The degree of valley polarization provides a promising route towards potential quantum applications [41–44]. In typical valleytronics materials, e.g., graphene, MoS_2 etc., the band gaps of distinct valleys are related by discrete symmetry (such as time reversal), making it difficult to create valley valve and filter devices. In anisotropic WTIs, the two valleys are not interrelated by any discrete symmetry. This unique feature provides an experimentally feasible pathway to independent tuning of the gaps at each valley, allowing for the construction of interesting valley devices. Below, we propose a valley filter and valley valve device based on an anisotropic WTI, as illustrated in Fig. 4(d). The regions I and V are source and drain, which can be fabricated by either isotropic or anisotropic thick WTIs. The regions II and IV are fabricated by thin anisotropic WTI films with tensile and compressive strain, respectively. The region III, made by a thick WTI, can relax the strain from region II to IV. Figures 4(e)–4(g) illustrate the working mechanism of the device. The valley valve is illustrated in Fig. 4(e). Because of momentum mismatch, the electron tunneling in the Y valley is forbidden, and the surviving X valley electrons in region III can hardly tunnel to region V. Furthermore, the only biased gate 1 leads to a Y valley filter [see Fig. 4(f)]. Both X and Y valley electrons can tunnel from region I to III while Y valley electrons are admitted after region IV. Similarly, an X valley filter is obtained by only biased gate 2, as shown in Fig. 4(g). Moreover, by appropriately tuning the bias of two separate gates, a 100% X valley polarization can be continuously switched to 100% Y valley polarization. To emphasize, this proposed device has two advantages: (i) the complete valley manipulation can be obtained by current experimental electric techniques; (ii) the magnitude of valley current is remarkable with low dissipation, protected by the robust transport properties of helical surface states.

Materials discussion.—The proposed model with emerging robust helical surface states could, in principle, be realized and probed in realistic $Z_2 = 0$ materials. Two candidate materials are noteworthy [45]. (1) Bismuth (111) film with a thickness of between 20 and 70 nm, where the robust helical surface states lead to several experimental observable phenomena. The surface bands can cross the Fermi level an odd number of times between two time-reversal invariant points, and consequently, weak antilocalization behavior is expected. From our model calculations [45], the effective energy gap is thickness dependent and on the order of a few tens of meV, suggesting that the proposed effects can be measured at $T \sim$ tens of K. Moreover, this prediction is also highly relevant to an unpublished experiment [46]. (2) The $(SnTe)_7(CaTe)_1(110)$ superlattice film with 0.1%–0.4% uniform c-axis tensile strain, with the thickness range of about 100–200 nm for a given strain ratio [45]. The effective energy gap is estimated to be around 1 meV.

Summary.—We demonstrate the emergence of robust helical edge (surface) states in both 2D and 3D anisotropic $Z_2 = 0$ systems. The anisotropy and finite size confinement play important roles in realizing such states. These emerging robust helical states lead to the revival of major features of $Z_2 = 1$ systems. In addition, the effective

energy gap for robust helical states can be engineered by tailoring sample size. These characteristics have potential applications as valley filter and valley valve under current experimental techniques.

We are grateful to Q. Niu, S. Q. Shen, L. Fu, and especially X. F. Jin for valuable discussions. This work was nan- cially supported by NBRPC (2011CBA00109, 2012CB921303, 2012CB821402, 2013CB921900, and 2014CB920901), Shanghai Super Computer, NSFC (91221302, 11274364, 11174009, and 11374219), and CPSF(2013T60020).

*jfeng11@pku.edu.cn
†xcxie@pku.edu.cn

[1] For recent reviews, see M. Z. Hasan and C. L. Kane, Rev. Mod. Phys. **82**, 3045 (2010);X.-L. Qi and S.-C. Zhang, Rev. Mod. Phys. **83**, 1057 (2011); Y. Ando, J. Phys. Soc. Jpn. **82**, 102001 (2013).
[2] C. L. Kane and E. J. Mele, Phys. Rev. Lett. **95**, 226801 (2005); **95**146802 (2005).
[3] M. König, S. Wiedmann, and C. Brüne, A. Roth, H. Buhmann, L. W. Molenkamp, X.-L. Qi, and S.-C. Zhang, Science **318**, 766 (2007).
[4] A. Roth, C. Brune, H. Buhmann, L. W. Molenkamp, J. Maciejko, X.-L. Qi, and S.-C. Zhang, Science **325**, 294 (2009).
[5] L. J. Du, I. Knez, G. Sullivan, and R.-R. Du, arXiv:1306.1925.
[6] C. Brüne, A. Roth, H. Buhmann, E. M. Hankiewicz, L. W. Molenkamp, J. Maciejko, X.-L. Qi, and S.-C. Zhang, Nat. Phys. **8** 486 (2012).
[7] H.-J. Zhang, C.-X. Liu, X.-L. Qi, X. Dai, Z. Fang, and S.-C. Zhang, Nat. Phys. **5**, 438 (2009).
[8] D. Hsieh, Y. Xia, L. Wray *et al.*, Science, **323**, 919 (2009).
[9] T. Hanaguri, K. Igarashi, M. Kawamura, H. Takagi, and T. Sasagawa, Phys. Rev. B **82**, 081305(R) (2010).
[10] J. Chen, H. J. Qin, F. Yang *et al.*, Phys. Rev. Lett. **105**, 176602 (2010).
[11] P. Roushan, J. Seo, C. V. Parker, Y. S. Hor, D. Hsieh, D. Qian, A. Richardella, M. Z. Hasan, R. J. Cava, and A. Yazdani, Nature (London) **460**, 1106 (2009).
[12] L. Fu, and C. L. Kane, Phys. Rev. B **76**, 045302 (2007); L. Fu, C. L. Kane, and E. J. Mele, Phys. Rev. Lett. **98**, 106803 (2007).
[13] B. H. Yan, L. Müchler, and C. Felser, Phys. Rev. Lett. **109**, 116406 (2012).
[14] P. Z. Tang, B. H. Yan, W. D. Cao, S.-C. Wu, C. Felser, and W. H. Duan, Phys. Rev. B **89**, 041409(R) (2014).
[15] G. Yang, J. W. Liu, L. Fu, W. H. Duan, and C. X. Liu, Phys. Rev. B **89**, 085312 (2014).
[16] X. Li, F. Zhang, Q. Niu, and Ji Feng, arXiv:1310.6598.
[17] L. Fu, Phys. Rev. Lett. **106**, 106802 (2011).
[18] T. H. Hsieh, H. Lin *et al.*, Nat. Commun. **3**, 982 (2012).
[19] R. Buczko and Ł. Cywiński, Phys. Rev. B **85**, 205319 (2012).
[20] S.-Y. Xu, C. Liu, and N. Alidoust, Nat. Commun. **3**, 1192 (2012).
[21] Y. Tanaka, Z. Ren, T. Sato, K. Nakayama, S. Souma, T. Takahashi, K. Segawa, and Y. Ando, Nat. Phys. **8**, 800 (2012).
[22] P. Dziawa, B. J. Kowalski *et al.*, Nat. Mater., **11**, 1023 (2012).
[23] B. Rasche, A. Isaeva, M. Ruck, S. Borisenko, V. Zabolotnyy, B. Büchner, K. Koepernik, C. Ortix, M. Richter, and J. van den Brink, Nat. Mater. **12**, 422 (2013).
[24] B. A. Bernevig, T. L. Hughes, and S.-C. Zhang, Science **314**, 1757 (2006).
[25] X.-L. Qi, Y. S. Wu, and S.-C. Zhang, Phys. Rev. B **74**, 085308 (2006).
[26] See the Supplemental Material at http://link.aps.org/supplemental/10.1103/PhysRevLett.112.176601, which includes Refs. [27–29] for details.
[27] D. N. Sheng, Z. Y. Weng, L. Sheng, and F. D. M. Haldane, Phys. Rev. Lett. **97**, 036808 (2006); D. J. Thouless, M. Kohmoto, M. P. Nightingale, and M. den Nijs, Phys. Rev. Lett. **49**, 405 (1982); M. Kohmoto, Ann. Phys. (N.Y.) **160**, 343 (1985).
[28] C. W. Groth, M. Wimmer, A. R. Akhmerov, J. Tworzydło, and C. W. J. Beenakker, Phys. Rev. Lett. **103**, 196805 (2009); J. T. Song, H. W. Liu, H. Jiang, Q.-F. Sun, and X. C. Xie, Phys. Rev. B **85**, 195125 (2012).
[29] A. MacKinnon and B. Kramer, Phys. Rev. Lett. **47**, 1546 (1981).
[30] B. Zhou, H.-Z Lu, R.-L. Chu, S.-Q. Shen, and Q. Niu, Phys. Rev. Lett. **101**, 246807 (2008);H.-Z. Lu, W.-Y Shan, W. Yao, Q. Niu, and S.-Q. Shen, Phys. Rev. B **81**, 115407 (2010).
[31] Y. Zhang, K. He, C.-Z. Chang, C.-L. Song *et al.*, Nat. Phys. **6** 584 (2010); A. A. Taskin, S. Sasaki, K. Segawa, and Y. Ando, Phys. Rev. Lett. **109**, 066803 (2012).
[32] S. Datta, *Electronic Transport in Mesoscopic Systems* (Cambridge University Press, Cambridge, England, 1995).
[33] H. Jiang, L. Wang, Q.-F. Sun, and X. C. Xie, Phys. Rev. B **80**, 165316 (2009).
[34] H. Jiang, Z. H. Qiao, H. W. Liu, J.-R. Shi, and Q. Niu, Phys. Rev. Lett. **109**, 116803 (2012).
[35] K.-I. Imura, M. Okamoto, Y. Yoshimura, Y. Takane, and T. Ohtsuki, Phys. Rev. B **86**, 245436 (2012).
[36] R. S. K. Mong, J. H. Bardarson, and J. E. Moore, Phys. Rev. Lett. **108**, 076804 (2012).
[37] Z. Ringel, Y. E. Kraus, and A. Stern, Phys. Rev. B **86**, 045102 (2012).
[38] K. Kobayashi, T. Ohtsuki, and K.-I. Imura, Phys. Rev. Lett. **110**, 236803 (2013).
[39] Y. Yoshimura, A. Matsumoto, Y. Takane, and K.-I. Imura, Phys. Rev. B **88**, 045408 (2013).
[40] C.-X. Liu, X.-L. Qi, H.-J. Zhang, X. Dai, Z. Fang, and S.-C. Zhang, Phys. Rev. B **82**, 045122 (2010).
[41] A. Rycerz, J. Tworzydło, and C. W. J. Beenakker, Nat. Phys. **3**, 172 (2007).
[42] D. Xiao, W. Yao, and Q. Niu, Phys. Rev. Lett. **99**, 236809 (2007).
[43] T. Cao, G. Wang, W. P. Han *et al.*, Nat. Commun. **3**, 887 (2012); D. Xiao, G. B. Liu, W. X. Feng, X. D. Xu, and W Yao, Phys. Rev. Lett. **108**, 196802 (2012); K. F. Mak, K. He, J. Shan, and T. F. Heinz, Nat. Nanotechnol. **7**, 494 (2012).
[44] J. Isberg, M. Gabrysch, J. Hammersberg, S. Majdi, K. K. Kovi, and D. J. Twitchen, Nat. Mater. **12**, 760 (2013).
[45] H. Jiang, M. Wu, X. Li *et al.* (to be published).
[46] K. Zhu, L. Wu, X. X. Gong, S. H. Xiao *et al.*, arXiv:1403.0066v1.